[Supplementary material]

Monte Verde II: an assessment of new radiocarbon dates and their sedimentological context

Mario Pino[1,2,*] & Tom D. Dillehay[3,4,5]

[1] Instituto de Ciencias de la Tierra, Universidad Austral de Chile, Valdivia, Chile

[2] Fundación para los Estudios Patrimoniales Pleistocenos de Osorno, Chile

[3] Department of Anthropology, Vanderbilt University, Nashville, USA

[4] Escuela de Arqueologia, Universidad Austral de Chile, Puerto Montt, Chile

[5] School for Advanced Research, Santa Fe, USA

[*] Author for correspondence ✉ mariopino@uach.cl

Radiocarbon methods

Thirty-nine AMS-based radiocarbon dates were obtained on plant, wood and charcoal fragments taken from a series of 10mm segments of Erwin Taylor's 0.945m core. An effort was made to select single-season or close to-single-season items for dating. Table S1 lists the series of conventional and calibrated AMS ages obtained on fragmentary amounts of plant tissue, wood, and charcoal from a series of 10mm increments both in Taylor and Pino's sediment cores. Organic fragments from each level were hand-picked from the dried sediment under magnification. According to Taylor's report, organic fragments from each level were hand-picked from the dried sediment under magnification. These materials were chemically pre-treated with 1M HCl at 90°C for 30 minutes to remove diagenetic carbonates and fulvic acids followed by treatment in 1M NaOH at 90°C in 30 min increments to solubilise humic acids. The NaOH treatment was continued until there was no colour in the solution at the end of a 30-minute treatment. Following the final NaOH treatment, samples were reacidified in 1M HCl at 90°C for at least 30 minutes and then treated with Millipore DI/UV ultrapure H_2O at 90°C for at least 30 minutes until a pH in the range between 5 and 7 was reached. The samples were then dried for at least 12 hours at 90°C. Samples were combusted to CO_2 and the CO_2 converted to a form of synthesised graphitic carbon (catalytically condensed graphitic carbon) using iron as the catalyst in the presence of H_2 at 500°C. The radiocarbon values were measured on an NEC 0.5MV accelerator mass spectrometer operating at the Keck Carbon Cycle AMS facility at the University of California, Irvine (Southon & Santos 2004). For all radiocarbon measurements, radiocarbon

infinite age blank samples and known age standards were pre-treated in the same manner as all unknown age samples being dated and measured at the same time as the unknowns. Radiocarbon ages are expressed using the Stuiver and Polach (1977) conventions and the calibrated radiocarbon ages were first calculated by Taylor and colleagues (2017) using the CALIB 7.1 algorithm and protocols (Stuiver *et al.* 2017), employing the southern hemisphere data set contained in SHCal13 (Hogg *et al.* 2013). The $\delta^{13}C$ values were obtained on a Finnegan MAT Delta Plus Isotope Radio Mass Spectrometer equipped with a Fisons 1500NC elemental analyser. Precision on the cited $\delta^{13}C$ values is $<\pm 0.1‰$ with reference to PDB.
In MP's MV-86b core, four radiocarbon ages were obtained. Two samples were analysed by DirectAMS—the methods of pretreatment and measurement of the samples are very similar to those already described above for Keck Carbon Cycle AMS facility at the University of California, Irvine—and another two in the same Keck Carbon Cycle AMS facility. The duplicate radiocarbon samples analysed from the two cores were averaged using standard techniques such as the arithmetic mean for age and for the square root of the sum of any squared individual errors. When all samples were analysed in triplicate, the pooled mean and the standard error were used. Afterwards, assays were calibrated using the CALIB Radiocarbon Calibration Execute Version 8.2, applying the SHCal20 curve (Stuiver & Reimer 1993; Hogg *et al.* 2020). The median probability age and the 94.5% (2σ) probability ages were extracted for each age. Next, the age and depth of the samples were related by a depth inverse Y-square root of X curve regression (Statgraphics Centurion XVII ©) (Figure S1). The regression model also was applied to the palaeoenvironmental interpretations

Radiocarbon data

Table S1. Radiocarbon dates of the 29 samples corresponding to Taylor's core after averaging the duplicate and triplicate samples (in black) and the four samples from the MV-86b core (in blue).

Lab no.	Depth (m)	$\delta^{13}C$ (‰)	Conventional age (in ^{14}C yr BP)	Median probability (cal yr BP)	94.5% range (cal yr BP)	Area under probability distribution
UCIAMS-120984	0.13–0.14	n/a	95±120	modern		
UCIAMS-120985	0.14–0.15	n/a	4385±125	4970	4610–5310	0.989
UCIAMS-120986	0.20–0.21	−30.2	9185±125	10 340	10 110–10 610	0.915
D-AMS 030320	0.27–0.30	n/a	9468± 44	10 660	10 510–10 780	0.964
UCIAMS-120987	0.29–0.30	n/a	10 520±140	12 350	11 930–12 730	1.000
UCIAMS-120988	0.49–0.50	−26.9	12 140±130	14 000	13 730–14 440	0.938
D-AMS 030321	0.56	n/a	12 094±54	13 920	13 800–14 060	1.000
UCIAMS-120989	0.59–0.60	−27.6	12 620±140	14 870	14 210–15 330	1.000
UCIAMS-165611	0.61–0.64	n/a	12 430±100	14 530	14 110–14 960	1.000
UCIAMS-119553*	0.69–0.70	−27.8	12 650±187	14 723	14 069–15 347	1.000
UCIAMS-119552	0.70–0.71	−29.1	12 650±135	14 950	14 270–15 400	1.000
UCIAMS-119551	0.71–0.72	−29.8	12 625±135	14 970	14 290–15 420	1.000
UCIAMS-119555	0.72–0.73	−30.2	12 785±135	15 200	14 810–15 660	0.954
UCIAMS-119550	0.73–0.74	−29.3	12 680±135	15 010	14 760 –15 470	0.756
UCIAMS-119549	0.74–0.75	−28.5	13 900±135	16 814	16 370–17 140	0.980
UCIAMS-119548	0.75–0.76	−28.4	13 980±135	16 930	16 530–17 340	1.000
UCIAMS-119547	0.76–0.77	−28.0	12 965±135	15 460	15 080–15 860	1.000
UCIAMS-119546	0.77–0.78	−26.9	12 630±135	14 900	14 240–15 340	1.000
UCIAMS-119545	0.78–0.79	−27.0	12 600±135	14 840	14 210–15 290	1.000
UCIAMS-117676	0.79–0.80	−27.5	12 580±130	14 787	14 2 10–15 250	1.000

UCIAMS-165612	0.80–0.81	n/a	12 635±45	15 010	14 820–15 190	0.953
UCIAMS-117675	0.80–0.81	−28.0	13 330±135	15 980	15 590–16 380	1.000
UCIAMS-117674	0.81–0.82	−28.0	12 625±130	14 890	14 260–15 320	1.000
UCIAMS-117673	0.82–0.83	−27.9	12 655±130	14 960	14 290–15 390	1.000
UCIAMS-117672	0.83–0.84	−28.2	12 680±130	15 010	14 770–15 460	0.767
UCIAMS-117671	0.84–0.85	−27.9	12 610±130	14 860	14 240–15 300	1.000
UCIAMS-117670	0.85–0.86	−28.7	12 560±130	14 830	14 240–15 280	1.000
UCIAMS-118281	0.86–0.87	n/a	12 585±130	14 800	14 220–15 260	1.000
UCIAMS-117669	0.87–0.88	−27.5	12 530±135	14 675	14 150–15 180	1.000
UCIAMS-117668**	0.89–0.90	−28.5	12 600 ±184	14 810	14 098–15 411	1.000
UCIAMS-116355***	0.90–0.91	−27.2	12 442±75	14 536	14 170–14 945	1.000
UCIAMS-116352****	0.91–0.92	−27.6	12 403±75	14 461	14 104–14 874	1.000
UCIAMS-116349*****	0.92–0.93	−27.6	12 602±75	14 907	14 782–15 198	0.691
UCIAMS-112450	0.93–0.94.5	n/a	12 435±125	14 540	14 080–15 020	1.000

* corresponds to the mean of UCIAMS-119553/120990.

** corresponds to the mean of UCIAMS-117668/116359/116358.

*** corresponds to the mean of UCIAMS-116355/116356/116357;

**** corresponds to the mean of UCIAMS-116352/116353/116354;

***** corresponds to the mean of UCIAMS-116349/116350/116351.

In the first case the error is equal to the square root of the sum of the squared individual errors; in the last four cases the mean was calculated as pooled mean and the error as standard error.

Modelled age

Figure 8 shows the modelled age, represented by the equation:

$$cal\ age = (\frac{132.63 - 767.334}{depth})^2$$

Since the P-value in the ANOVA calculations is less than 0.05, there is a statistically significant relationship between age and depth (at the 95% confidence level). The statistical adjustment for the freedom degree R-Squared calculation indicates that the fitted model explains 89.6 per cent of the variability in age. The correlation coefficient is equal to −0.9482, indicating a relatively strong relationship between the variables.

Simple Regression - cal age vs. depth

Dependent variable: cal age
Independent variable: depth
Squared-Y reciprocal-X model: Y = sqrt(a + b/X)
Number of observations: 33

Coefficients

Parameter	Least Squares Estimate	Standard Error	T Statistic	P-Value
Intercept	2.69568E8	5.86181E6	45.9872	0.0000
Slope	-3.44308E9	2.71485E8	-12.6824	0.0000

Analysis of Variance

Source	Sum of Squares	Df	Mean Square	F-Ratio	P-Value
Model	6.28568E16	1	6.28568E16	160.84	0.0000
Residual	1.21147E16	31	3.90796E14		
Total (Corr.)	7.49715E16	32			

Correlation Coefficient = -0.915647
R-squared = 83.841 percent
R-squared (adjusted for d.f.) = 83.3197 percent
Standard Error of Est. = 1.97686E7
Mean absolute error = 1.25276E7
Durbin-Watson statistic = 0.975463 (P=0.0004)
Lag 1 residual autocorrelation = 0.493787

The StatAdvisor

The output shows the results of fitting a squared-Y reciprocal-X model to describe the relationship between cal age and depth. The equation of the fitted model is

cal age = sqrt(2.69568E8 - 3.44308E9/depth)

Since the P-value in the ANOVA table is less than 0.05, there is a statistically significant relationship between cal age and depth at the 95.0% confidence level.

The R-Squared statistic indicates that the model as fitted explains 83.841% of the variability in cal age. The correlation coefficient equals -0.915647, indicating a relatively strong relationship between the variables. The standard error of the estimate shows the standard deviation of the residuals to be 1.97686E7. This value can be used to construct prediction limits for new observations by selecting the Forecasts option from the text menu.

The mean absolute error (MAE) of 1.25276E7 is the average value of the residuals. The Durbin-Watson (DW) statistic tests the residuals to determine if there is any significant correlation based on the order in which they occur in your data file. Since the P-value is less than 0.05, there is an indication of possible serial correlation at the 95.0% confidence level. Plot the residuals versus row order to see if there is any pattern that can be seen.

Figure S1. Results of fitting a squared-Y reciprocal-X model to describe the relationship between cal age and depth (obtained from the Statgraphics Centurion XVII © outputs).

Sedimentological observations and interpretations

In July 2012, two sediment cores were obtained 40m north of the Monte Verde II site using a modified Livingston device. After a first examination of the sediments in the core, in 2014 we decided to excavate a pit (MV-86b) in the same position as the original Pino core. Undisturbed, non-cultural sediments were extracted. After extraction and labelling, the columns were packed in plastic wrap to be taken to the Sedimentology Laboratory of the Universidad Austral de Chile. Here, the description of the macroscopic sedimentological characteristics was carried out as a complement to the field description. A textural analysis was conducted by taking with a syringe cut in its apex, 2000mm^3 of sediment every 20 or 40mm of the column (20 samples: Table S2). Samples were subjected to the determination of loss by ignition (LOI), to determine the content of organic matter and carbonates (Dean 1974; Bengtsson & Enell 1986). Generally, the results of a granulometric analysis are expressed in per cent values. A problem resides in the fact that percentages are mathematically related, because if one component per example—sand—decreases by a natural reason, the others also suffer an artefactual modification. For this reason, samples were taken of a constant volume and the granulometric fractions in mass were extracted (Table S2). A wet sieving method was used to separate 20 samples in gravel, sand and mud fractions (>2mm, 2mm to 62.5μ and <62.5μ, respectively; Folk 1980), and LOI methods to measure the organic carbon matter in each fraction (Heiri *et al.* 2001). One of the cores was sent to Taylor (the Taylor core). Table S2 shows the granulometric/textural classification of the 20 samples collected from the MV-86b column. Four components (siliciclastic gravel, sand, mud and peat) allow us to identify five sediment types. Siliciclastic mud is the main compound (muddy peat, muddy sandy peat and muddy peaty sand; 11, three and four samples, respectively). Another two samples correspond to mixtures without siliciclastic mud, located near the base of the sedimentary column, a peaty ruditic sand and a sandy ruditic peat. At the base of the column one sample (20) include a high content of gravel. The next seven samples contain sand as a principal or important component (samples 19–14, 0.79–0.63m depth, 15 110–14 510 cal BP). Only one sample include an important item of gravel (sample 14, 35%, 0.63m depth, 14 500 cal BP). In this first group the fine sediment fraction alternate between peat and siliciclastic mud. From 0.56m deep (14 000 BP) to the top, the next group of 12 samples are muddy peat, except for sample 6 (approximately 0.39m, *c*. 12 800 cal BP) because a peak of siliciclastic sand.

Figure S2 shows the mass content of the siliciclastic gravel and of the total sand and mud, subdivided in the siliciclastic and organic fractions. The siliciclastic ruditic fraction has a maximum in the deepest sample (0.83m) and a second minor peak in the depth 0.63m. All other samples from 0.59m to the top do not have this coarse sediment. The total sand, obtained by adding the siliciclastic and organic fractions, is the most important item in the samples, reaching very similar quantities between the base (the MV-7 interphase) and the 0.39m deep, with a drop-in depth of 0.36m, and from here showed a plateau near 0.03g (grams) to the top (Figure S2; Table S2). Both components have a different trend. The siliciclastic fraction increases from the base to the 0.80m sample, then remain stable in a plateau until sample at 0.63m and from this drop to the top of the sequence, with a minor peak at 0.39m.

The mass of the organic sand made a mirror to the former component until sample at 0.39m. Then originate a minimum at 0.36m and from this sample increase to the top of the column with a mass of 1.24g, the highest of the whole samples and fractions. Finally, the total mud fraction mass is near 0.10g between the base and sample 14 at 0.63m, then increase consistently to 0.34m, then decrease to a minimum in the next 20mm, then increase again to the top until it reaches 0.53g. Both siliciclastic and organic mud fractions have a very similar trend, but the mass of the latest is more important from the sample at 0.59m, with a opposite trend only in the last 10mm at the top, with 0.42 and 0.11g, respectively (Figure S2; Table S2).

We interpret the siliciclastic gravel fraction (pebble diameter) at the base of the column (around 0.83m; Table S2) as a result of an erosional process which affects layers corresponding to the member SCH-4 of the Salto Chico Formation, which outcrops in a terrace north of the pit (Pino 1989). If the gravel fraction was related to a depositional event, simultaneously, there should also be an increase in the very coarse or coarse sand fraction. For that reason, in the absence of sand, the most viable process involved in the gravel deposit is a lag deposition. This is a 'stone pavement' laid over the top of SCH-4. The formation of this pervasive gravel bed has previously been attributed to wind and water erosion, implying that gravel is transiently concentrated on the land surface (Wells *et al*. 1995). Fire activity and heavy rainfall could have promoted erosive processes during post-fire events. It is possible to interpret the effect of local fires that would enhance erosion of the high terrace corresponding to the top of SCH-4 and the production of gravel lag deposits in the MV-86b pit (J. Martel, *pers. comm*.).

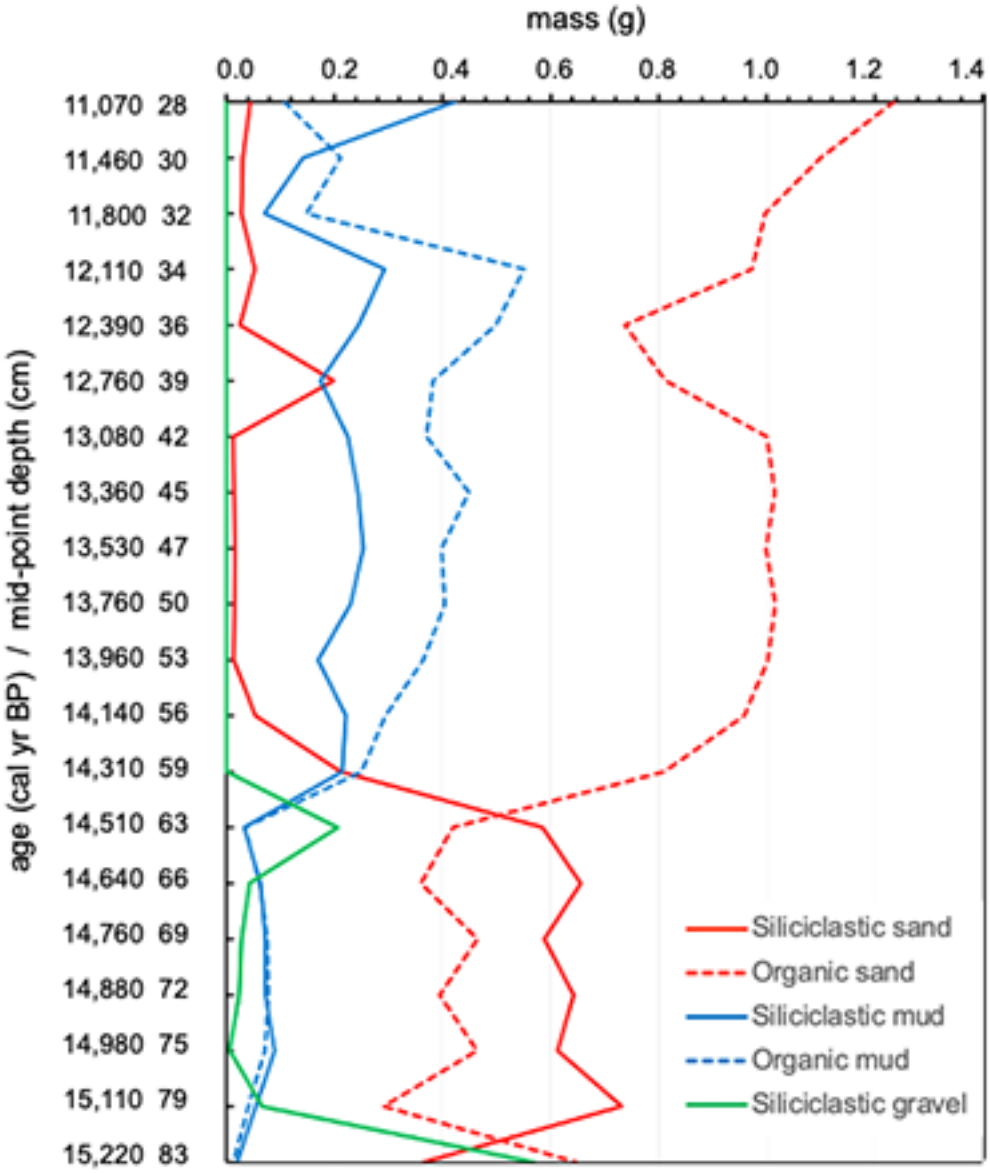

Figure S2. Temporal variation of textural and granulometric variables (expressed as mass in g) of the MV-5 peat layer (MV-86b column).We observe three strong sedimentological changes: the first is at the base near the interphase with MV-7 (increase of siliciclastic sand and decrease of siliciclastic gravel); the second, at 63 cm deep (increase of all organic fraction, decrease of the siliciclastic sand, a minor siliciclastic gravel peak); and the last occurs at 0.34–0.36m deep (organic sand begins to increase after a minimum and the organic mud reach the maximum peak of all the column) (image by M. Pino)

The decrease of gravel is accompanied by an increase of siliciclastic sand fraction to values of 0.62g, which remains constant up to a depth of around 0.64m (*c*. 14 500 cal BP). Here, a second and final gravel peak occurs, smaller than that at the base of the column (0.6 *vs* 0.2g). This second maximum of ruditic sediments coincides with the beginning of the decline in

sand content in the upper layers, near 14 500 cal BP, which may be related to a lag deposit after a short rain event. The phase of decreasing sand content to zero values occurs gradually up to a depth of 0.56m (Figure S2; Table S1 & S2; 14.0 kya). This change in textural composition occurs in the zone of the slope change of the age model (see Figure 5).

From the base of column MV-86b up to 0.42m (13.0 kya), the organic matter of sand equivalent diameter follows inversely the trend of the siliciclastic sand fraction. This trend is real and not an artifact of data calculations, probably produced by the alternation of rhexistasis and biostasis cycles (Erhart 1956; Chellat *et al.* 2018). Between 0.83 and 0.64m deep, the inorganic part of the sand dominates, which originates the dominance of muddy peaty sand sediments in the lower part of the stratigraphic column (Table S2; Figure S2). From 0.64m upwards, the dominant sediment is carbonaceous organic matter of sand diameter, in addition to the sustained increase of siliciclastic and organic mud, which gives the bog-like characteristics to the sedimentation basin. Unlike sand fractions, siliciclastic and organic (fine vegetal and charcoal debris <63μ) mud fractions follow the same pattern. This would imply that both fractions have the same source and deposition process. This means that a low-energy deposition process (biostasis) dominated in an environment of high plant production once the erosional processes (rhexistasis) on the terrace north of the marsh came to an end. In geological terms, the dominant organic deposition is interrupted at 0.39m (*c.* 12 760 cal BP) with the deposition of unique sandy level (Figures 4 & 5; Table S2). During this period, fire activity drastically decreased (14 000–12 200 cal BP), which is concomitant with the increment of the *Nothofagus dombeyi* type. Towards the top of the column there is a total absence of siliciclastic sand, dominate with mass increases and decreases both mud fractions and sand of organic composition. Analysis of the MV-86b column did not include the modern soil in MV-I, dated at 95±20 cal BP (Table S1)

In summary, the sedimentological analysis allows us to identify three key moments of change in the bog. The first is registered at base of the MV-86b column (samples 19 and 20; Table S2; Figure S2) between 15 500–15 000 cal BP (0.83m deep) where the mass of the siliciclastic gravel is highest. Also, the siliciclastic and the organic sand show an opposite trend, with the former increases as the later decrease. This situation is interpreted as a moment of erosion that deposited the gravel as a lag associated with a siliciclastic sand deposition with low contents of organic sand. This episode could correspond to the formation of the incision of the main terrace by the Chinchihuapi creek (Dillehay *et al.* 2015), which would have allowed the later deposition of the Monte Verde Formation. The sample, at a

depth of 0.83m, however, probably represents the final stage of this process before 15 500 cal BP, probably around 1000 years before the MV-II human occupation (Dillehay *et al.* 2015). The second key change occurs after the disappearance of the gravel at the depth of 0.63m (*c*. 14 500 cal BP; Table S2; Figures 5 & S2). It is possible to observe trends of siliciclastic and organic sand mass, which increases the organic mass. Since the organic values are expressed as mass and the organic matter has a density of 0.7g cm^{-3}, the volume of organic matter should correspond to about 75 per cent of the samples in this column (Pino *et al.* 2019). This is interpreted as the establishment of a well-developed and expanding as was described in sections of MV–5 (Pino 1989; Figure 3). This second key change is related to a change of climatic/vegetational conditions. This sedimentological change coincides with the human settlement at MV-II (Dillehay 1989a, 1989b; Dillehay & Pino 1989). The sedimentological data shows that a shallow bog and its vegetational resources (Ramirez 1989) were present approximately 40m from the site, shortly before the human settlement.

The third change is detected at a depth of 0.34–0.36m (*c*. 12 000 cal BP). Here, the organic sand begins to increase, and the organic mud reaches a maximum peak in the column. This sediment is likely the equivalent of the brown peat MV-4 layer interfingering with the base of MV-3 (Figure 3), as described by Pino (1989). Here also, this sedimentological change is related to a change of climatic/vegetational conditions. According to Dillehay and Pino (1989), layer MV-3 was dated between 8270±110 and 4750±90 BP (equivalent today to 9.2 and 5.4 kyr cal BP) at site MV-II. Thus chrono-stratigraphically, layer MV-3 is represented in column MV-86b and Taylor's core from 0.21m to the top. Layer MV-4 (fluvial gravel in the *locus typicus* of the Monte Verde Formation; Pino 1989; Dillehay & Pino 1989) (section A in Figure 3) was dated once at 8030±130 BP). In Figure 3, it can be seen that the fluvial facies of MV-4 is gradually wedging northward, possibly interfingering with the peat in the MV-86b column/ET cores.

We do not know the cause of the erosive process that originated the elongated depression in Monte Verde where the layers of the homonymous formation were deposited, and the human settlement took place. The unconformity between the upper layers of SCH-4 (MV-7) and the MV-5 layer is not only a geological feature (see the red line in the Figure 3) but corresponds to a surface that was used by the MV-II inhabitants. In general, the geomorphological erosive processes are associated with a lowering of the base level, in this case the elevation difference between the bed of Chinchihuapi creek and its effluent, the Maullín River Estuary. But at the end of the LGM (Bennett *et al.* 2000), the sea level and therefore the base level of the

Maullin River were rising. If the cause of the relative submergence of the Maullin River Estuary bottom is not related to climatic change, then the possibility arises that the reason could be a neotectonic process. In southern Chile, megathrust earthquakes are frequent and have caused continental syntectonic subsidence (submergence) of the order of a few meters, every *c*. 300 years (Cisternas *et al.* 2005).

The depth of the columns in the MV-86b and Taylor cores do not match perfectly with the depths of column 32, probably because of the undulating paleo-surface of SCH-4 (section B in Figure 3). By combining the old and new radiocarbon dates, it is now possible to reinterpret the equivalence of two different coloured peats and the gravel intercalation between them (between columns 25 to 32; see Figure 3). Thus, the approximately 0.94m deep column in the MV-86b and ET cores are correlated with layers MV-6 to MV-3 (Figure 3). At 0.39m depth (*c*. 12 800 cal BP) an isolated peak of siliciclastic sand was detected, which does not correlate with the figures of organic sand and total mud. Dillehay and Pino (1989) obtained an age of 10 860±130 BP to date the top of the MV-5 layer. The actual calibration is 12 800±130 cal BP (Stuiver & Reimer 1993; Hogg *et al*. 2020).

As mentioned earlier, based on the sea level at the end of the Pleistocene and on the location and topography of the Monte Verde (Dillehay *et al.* 2015), the ocean never reached the site during the last glacial cycle, despite those who have argued that the radiocarbon dates at MV-II are due to the effect of marine materials (e.g. as proposed by Taylor in his research proposal, cited both above and by Dickinson (2011), who cherry-picked erroneous geological data to suggest the same). Over the past four decades, there have been numerous attempts by 'Clovis first' proponents to dismiss the MV-II, including recent claims that the artefacts are unprovenanced (Fiedel 2013), despite their precise provenance numbers being listed numerous times for all artefacts and features in the thin, intact MV-II habitational surface and that the site's artefacts were found after ice sheets melted and later were transported to the site, making them younger that their radiocarbon dated age (Andersen 2021). These and other desperate attempts to dismiss the Monte Verde and other legitimate pre-Clovis sites, like the brother site Pilauco (Pino *et al.* 2019), will continue as long as there are supporters of the 'Clovis first' hypothesis.

Table S2. Depth and textural/granulometric composition and classification of the 20 sediment samples analysed. All the data are presented in grams. Dates are calculated from the age regression model and rounded to the nearest ten, using the statistical model cal age = (132.63−767.334/depth)^2

Sample no.	Depth range (m)	Depth midpoint (m)	Age (cal yr BP)	Total sand	Siliciclastic sand	Organic sand	Total mud	Siliciclastic mud	Organic mud	Total gravel	Total organic	Sediment type
1	0.270–0.290	0.28	11 070	1.28	0.04	1.24	0.53	0.42	0.11	0.00	1.34	Muddy peat
2	0.290–0.301	0.30	11 460	1.13	0.03	1.10	0.35	0.14	0.21	0.00	1.31	Muddy peat
3	0.310–0.330	0.32	11 810	1.02	0.03	1.00	0.22	0.07	0.15	0.00	1.14	Muddy peat
4	0.330–0.350	0.34	12 110	1.03	0.05	0.97	0.84	0.29	0.55	0.00	1.52	Muddy peat
5	0.35.0–0.375	0.36	12 390	0.76	0.02	0.74	0.74	0.25	0.50	0.00	1.24	Muddy peat
6	0.375–0.405	0.39	12 760	1.01	0.20	0.81	0.56	0.17	0.38	0.00	1.20	Muddy sandy peat
7	0.405–0.435	0.42	13 080	1.01	0.01	1.00	0.59	0.22	0.37	0.00	1.37	Muddy peat
8	0.435–0.460	0.45	13 360	1.03	0.01	1.01	0.69	0.24	0.45	0.00	1.46	Muddy peat
9	0.460–0.480	0.47	13 530	1.01	0.02	1.00	0.65	0.25	0.40	0.00	1.40	Muddy peat

10	0.480–0.515	0.50	13 760	1.03	0.02	1.02	0.63	0.23	0.40	0.00	1.42	Muddy peat
11	0.515–0.545	0.53	13 960	1.02	0.01	1.00	0.53	0.17	0.36	0.00	1.37	Muddy peat
12	0.545–0.575	0.56	14 140	1.01	0.05	0.96	0.52	0.22	0.29	0.00	1.25	Muddy peat
13	0.575–0.610	0.59	14 310	1.02	0.21	0.81	0.46	0.21	0.25	0.00	1.06	Muddy sandy peat
14	0.610–0.640	0.63	14 510	1.00	0.58	0.42	0.07	0.03	0.04	0.21	0.45	Peaty ruditic sand
15	0.640–0.670	0.66	14 640	1.02	0.66	0.36	0.13	0.06	0.06	0.04	0.42	Muddy peaty sand
16	0.670–0.700	0.69	14 760	1.05	0.59	0.46	0.15	0.07	0.08	0.03	0.54	Muddy sandy peat
17	0.700–0.730	0.72	14 880	1.04	0.64	0.40	0.15	0.07	0.08	0.02	0.47	Muddy peaty sand
18	0.730–0.765	0.75	14 980	1.08	0.61	0.46	0.16	0.09	0.07	0.01	0.54	Muddy peaty sand
19	0.765–0.805	0.79	15 110	1.02	0.73	0.29	0.10	0.05	0.04	0.07	0.33	Muddy peaty sand
20	0.805–0.840	0.83	15 224	1.01	0.37	0.65	0.03	0.02	0.01	0.57	0.66	Sandy ruditic peat

References

ANDERSEN, R. 2021. The search for America's Atlantis. *The Atlantic*, 7 September 2021. Available at https://www.theatlantic.com/magazine/archive/2021/10/prehistoric-america-atlantis/619819/ (accessed on 9 May 2022).

BENGTSSON, L. & M. ENELL. 1986. Chemical analysis, in B.E. Berglund (ed.) *Handbook of Holocene palaeoecology and palaeohydrology*: 423–51. Chichester: Wiley.

BENNETT, K.D., S.G. HABERLE & S.H. LUMLEY. 2000. The last glacial-Holocene transition in southern Chile. *Science* 290: 325–28. https://doi.org/10.1126/science.290.5490.325

CHELLAT, S. *et al*. 2018. Molluscan and sedimentological sequences of the Late Quaternary deposits of Morsott region (NE Algeria) and their paleoenvironmental implication. *Bulletin de la Société Géologique de France* 189: 17. https://doi.org/10.1051/bsgf/2018016

CISTERNAS, M. *et al*. 2005. Predecessors of the giant 1960 Chile earthquake. *Nature* 437: 404–407. https://doi.org/10.1038/nature03943

DEAN, JR, W.E. 1974. Determination of carbonate and organic matter in calcareous sediments and sedimentary rocks by loss on ignition: comparison with other methods. *Journal of Sedimentary Petrology* 44: 242–48. https://doi.org/10.1306/74D729D2-2B21-11D7-8648000102C1865D

DICKINSON, W.R. 2011. Geological perspectives on the Monte Verde archeological site in Chile and pre-Clovis coastal migration in the Americas. *Quaternary Research* 76: 201–10. https://doi.org/10.1016/j.yqres.2011.06.011

DILLEHAY, T.D. 1989a. Monte Verde. *Science* 245: 1436. https://doi.org/10.1126/science.245.4925.1436.a

– 1989b. Overviews of site setting and excavation, in T. Dillehay (ed.) *Monte Verde: a Late Pleistocene settlement in Chile. Volume 1: palaeoenvironment and site context*: 45–51. Washington, D.C.: Smithsonian Institution.

DILLEHAY, T.D. & M. PINO. 1989. Stratigraphy and chronology, in T. Dillehay (ed.) *Monte Verde: a Late Pleistocene settlement in Chile. Volume 1: palaeoenvironment and site context*: 133–46. Washington, D.C.: Smithsonian Institution.

DILLEHAY, T.D *et al*. 2015. New archaeological evidence for an early human presence at Monte Verde, Chile. *PLoS ONE* 10: e0145471. https://doi.org/10.1371/journal.pone.0141923

ERHART, H. 1956. *La genèse des sols en tant que phénomène géologique: esquisse d'une théorie géologique et géochimique, biostasie et rhexistasie*. Paris: Masson.

FIEDEL, S. 2013. Is that all there is? The weak case for pre-Clovis occupation of Eastern North America, in J.A.M. Gingerich (ed.) *The Eastern Fluted Point tradition*: 333–54. Salt Lake City: University of Utah Press.

FOLK, R.L. 1980. *Petrology of sedimentary rocks*. Sutton: Hemphill.

HEIRI, O., A.F. LOTTER & G. LEMCKE. 2001. Loss on ignition as a method for estimating organic and carbonate content in sediments: reproducibility and comparability of results. *Journal of Paleolimnology* 25: 101–10. https://doi.org/10.1023/A:1008119611481

HOGG, A.G. *et al*. 2013. SHCal13 Southern Hemisphere calibration, 0–50 000 years cal BP. *Radiocarbon* 55: 1889–903. https://doi.org/10.2458/azu_js_rc.55.16783

– 2020. SHCal20 Southern Hemisphere calibration, 0–55 000 years cal BP. *Radiocarbon* 62: 759–78. https://doi.org/10.1017/RDC.2020.59

KOPP, R.E. *et al*. 2009. Probabilistic assessment of sea level during the last interglacial stage. *Nature* 462: 863–67. https://doi.org/10.1038/nature08686

LOMNITZ, C. 2004. Major earthquakes of Chile: a historical survey, 1535–1960. *Seismological Research Letter* 75: 368–78. https://doi.org/10.1785/gssrl.75.3.368

PINO, M. 1989. Regional and site geology, in T. Dillehay (ed.) *Monte Verde: a Late Pleistocene settlement in Chile. Volume 1: palaeoenvironment and site context*: 89–132. Washington, D.C.: Smithsonian Institution.

PINO, M. *et al*. 2019. Sedimentary record from Patagonia, southern Chile supports cosmic-impact triggering of biomass burning, climate change, and megafaunal extinctions at 12.8 ka. *Scientific Reports* 9: 4413. https://doi.org/10.1038/s41598-018-38089-y

RAMIREZ, C. 1989. Macrobotanical remains, in T. Dillehay (ed.) *Monte Verde: a Late Pleistocene settlement in Chile. Volume 1: palaeoenvironment and site context*: 147–70. Washington, D.C.: Smithsonian Institution.

SOUTHON J.R. & G.M. SANTOS. 2004. Ion source development at KCCAMS, University of California, Irvine. *Radiocarbon* 46: 33–39. https://doi.org/10.1017/S0033822200039321

STUIVER, M. & H.A. POLACH. 1977. Discussion reporting of 14C data. *Radiocarbon* 19: 355–63. https://doi.org/10.1017/S0033822200003672

STUIVER, M. & J.P. REIMER. 1993. Extended ^{14}C data base and revised CALIB 3.0 ^{14}C age calibration program. *Radiocarbon* 35: 215–30. https://doi.org/10.1017/S0033822200013904

STUIVER M., P.J. REIMER & R.W. REIMER. 2017. CALIB 7.1. Available at: http://calib.org (accessed 6 September 2017).

– 2021. CALIB 8.2. Available at: http://calib.org (accessed 20 January 2021).

TAYLOR, R.E. & O. BAR-YOSEF. 2014. *Radiocarbon dating: an archaeological perspective*. Walnut Creek (CA): Left Coast.

WELLS, S.G., L.D. MCFADDEN, J. POTHS & C.T. OLINGER. 1995. Cosmogenic ^{3}He surface-exposure dating of stone pavements: implications for landscape evolution in deserts. *Geology* 23: 613–16. https://doi.org/10.1130/0091-7613(1995)023%3C0613:CHSEDO%3E2.3.CO;2